Bioconjugated Iron Oxide Nanocubes: Synthesis, Functionalization, and Vectorization

Laura Wortmann,[†] Shaista Ilyas,[†] Daniel Niznansky,[‡] Martin Valldor,[§] Karim Arroub,[†] Nadja Berger,[∥] Kamil Rahme,[#] Justin Holmes,[⊥] and Sanjay Mathur*[,†,∇]

[†]Institute of Inorganic Chemistry, University of Cologne, Greinstrasse 6, Cologne 50939, Germany

[‡]Department of Inorganic Chemistry, Faculty of Science, Charles University in Prague, Hlavova 8, 128 43 Praha 2, Czech Republic

[§]Max-Planck-Institut für Chemische Physik fester Stoffe, Nöthnitzer Strasse 40, 01187 Dresden, Germany

[∥]Lehrstuhl für Organische Chemie II, Ruhr Universität Bochum, Universitätsstrasse 150, 44801 Bochum, Germany

[⊥]Materials Chemistry & Analysis Group, The Tyndall National Institute at University College Cork, Cork, Ireland

[#]Department of Sciences, Faculty of Natural and Applied Science, Notre Dame University (Louaize), Zouk Mosbeh, Lebanon

[∇]International Research Center for Renewable Energy, Xian Jiaotong University Xian, Shaanxi 710049, PR China

S *Supporting Information*

ABSTRACT: A facile bottom-up approach for the synthesis of inorganic/organic bioconjugated nanoprobes based on iron oxide nanocubes as the core with a nanometric silica shell is demonstrated. Surface coating and functionalization protocols developed in this work offered good control over the shell thickness (8−40 nm) and enabled biovectorization of SiO_2@Fe_3O_4 core−shell structures by covalent attachment of folic acid (FA) as a targeting unit for cellular uptake. The successful immobilization of folic acid was investigated both quantitatively (TGA, EA, XPS) and qualitatively (AT-IR, UV−vis, ζ-potential). Additionally, the magnetic behavior of the nanocomposites was monitored after each functionalization step. Cell viability studies confirmed low cytotoxicity of FA@SiO_2@Fe_3O_4 conjugates, which makes them promising nanoprobes for targeted internalization by cells and their imaging.

Folic Acid

KEYWORDS: *bioconjugated nanoprobes, iron oxide-silica core−shell particles, magnetic properties, folic acid, cytotoxicity*
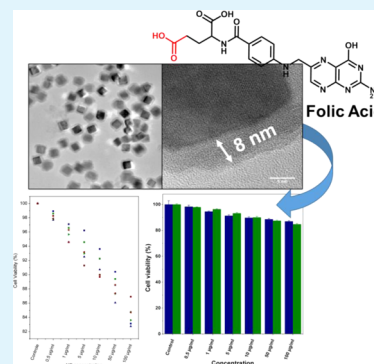
■ INTRODUCTION

Bioconjugated nanostructures combining two different modalities, such as therapeutic and diagnostic functions, are witnessing ever-increasing attention as a viable approach for fabricating new multifunctional materials with potential applications in various fields.[1−5] The combination of iron oxide nanoparticles with a physiologically inert silica shell offers controllable magnetic behavior, low cytotoxicity, and a chemically responsive surface that can be activated by carbodiimide,[6−8] click,[9−12] or other coupling chemistry protocols.[13−15] Given their bioconducive size and benign surface chemistry, such core−shell particle configurations are of particular interest for therapeutic and diagnostic applications such as drug delivery systems[16−19] and magnetic resonance imaging (MRI).[20−22] Although a large body of data is available on the synthesis and characterization of iron oxide−silica nanocomposites[23−31] strict control over nanoparticle size, chemical composition, and colloidal stability of nanoparticle dispersion remains a synthetic challenge. Especially, the understanding of the surface chemistry, for instance, physical versus chemical linkage of functional molecules, numerical coverage density, and analytical estimation of the number and type of groups present on the nanoparticle surface, is in its infancy.

Among cell specific targets, folic acid (FA) has been investigated as an active targeting ligand for cancer therapy and diagnosis, but the final translation to clinical use has not been successfully demonstrated so far.[32−34] This can be explained by the fact that although folic acid has a high affinity toward specific receptors (FR), which are overexpressed in almost 40% of human cancer cells,[35,36] the expression of FR(+) is patient-dependent and specific for each type of cancer.[37] Therefore, possible FR(+) expression needs to be verified for each patient. Fischer et al.[38] proposed a folate-targeted imaging modality to identify FR-positive patients. This approach would help in personalized medicine to screen FR-positive patients before the treatment and will help to demonstrate the application potential of such strategies. In one of our previous studies, we have also demonstrated that similar nanoconstructs are actively assimilated by endocytosis from oral cancer cells

(SKOV-3),[39] leading to the assumption that FA@SiO$_2$@Fe$_3$O$_4$ nanocomposites are a promising tool for cancer therapy.

Herein, we report the synthesis of folic acid-conjugated SiO$_2$@Fe$_3$O$_4$ core—shell structures and their cytotoxicity studies. For growing a homogeneous silica shell, monodisperse iron oxide nanoparticles with high colloidal stability are crucial to avoid agglomeration as well as the formation of multiparticle cores.[40] Cube-shaped α-Fe$_2$O$_3$ nanoparticles accessible by a facile solvothermal process[41] show high dispersibility and minimal magnetic dipole—dipole interactions caused by their antiferromagnetic nature that consequently alleviates the coating process due to a lower degree of agglomeration. For a conformal shell formation, a two-step coating procedure based on the condensation of silicic acid with basic iron oxide was first used to anchor —Si(OH)$_3$ groups (step 1) followed by the further growth and formation of the silica shell by condensation of tetraethylorthosilicate (step 2) toward the silanol groups rooted on the nanoparticle surface. Subsequently, surface functionalization by covalent attachment of amine groups generated via (3-aminopropyl)trimethoxysilane (APTMS) and FA was performed. Preliminary cytotoxicity studies revealed the low harmful effect of our hybrid nanoparticles, thereby pointing out the need for further investigations.

■ EXPERIMENTAL SECTION

Materials. All reagents and solvents were of analytical grade and used without further purification. Iron(III)nitrate nonahydrate (Fe-(NO$_3$)$_3$·9H$_2$O), ammonium hydroxide solution (28–30%), tetraethylorthosilicate (TEOS), N-hydroxysuccinimide (NHS), N,N'-dicyclohexylcarbodiimide (DCC), folic acid (FA), and 3-(4,5-dimethylthiazol-2-yl)-2,5-diphenyltetrazolium bromide (MTT) were purchased from Sigma-Aldrich. Dimethyl sulfoxide (DMSO) and dimethylformamide (DMF) were obtained from Fischer Scientific and poly(N-vinyl-2-pyrrolidone) MW = 55.000 (PVP) and (3-aminopropyl)-trimethoxysilane (APTMS) from Acros Organics. Phosphate-buffered saline (PBS) and Dulbecco's modified Eagle's medium (DMEM) were obtained from Gibco.

General Synthesis of Amine-Activated SiO$_2$@Fe$_3$O$_4$ Nanovectors. Cube-shaped α-Fe$_2$O$_3$ nanoparticles were synthesized following the reaction reported by Zheng et al.[41] For this purpose, 289 mg (0.571 mmol) of Fe(NO$_3$)$_3$·9H$_2$O was dissolved in 25.7 mL of DMF and subsequently 628 mg (0.011 mmol) of PVP was added. The solution was then transferred into a 50 mL Teflon-lined stainless autoclave and heated at 180 °C for 30 h. After cooling the autoclave down to room temperature, the particles were precipitated by centrifugation and washed several times with water and ethanol to remove any excess of the capping agent. Afterward, the particles were dried in a vacuum oven at 60 °C for 6 h. For the coating process, 120 mg of dried α-Fe$_2$O$_3$ nanoparticles was homogeneously redispersed in 180 mL of water by sonication for 20 min. Following this, 1.2 mL of silicic acid solution [SiO$_x$(OH)$_{4-2x}$]$_n$ was added, which was prepared in advance by a controlled hydrolysis of 0.65 mL of TEOS in 5 mL of distilled water catalyzed by adding 1 M HCl to adjust the pH to 4. The solution was mixed homogeneously by magnetic agitation for 30 min, 1.2 mL of NH$_4$OH (28%) was added, and after aging the reaction for 3 h, the particles were collected by centrifugation and redispersed in 120 mL of ethanol. In the next step, 0.24 mL of TEOS was added to the solution, followed by the addition of 1.95 mL of NH$_4$OH (28%). The reaction was continued for 3 h under continuous stirring. To increase the shell thickness further, 0.24 mL of TEOS was added and the reaction mixture was aged overnight. The silica-coated particles were separated from the solution by centrifugation and washed with ethanol several times. The hematite core of the dried particles was reduced in an oven using forming gas (5% H$_2$/95% Ar) at 350 °C for 1 h with a heating rate of 10 °C/min. The surface of Fe$_3$O$_4$—SiO$_2$ nanoparticles was further modified using APTMS. For this purpose, 200 mg of dried

SiO$_2$@Fe$_3$O$_4$ was poured in 200 mL of dry toluene under inert atmosphere. To the reaction mixture was added 2.0 mL of APTMS, and the reaction was mechanically stirred overnight. Afterward, the solution was heated to reflux for 6 h, and the particles were separated magnetically and washed several times with ethanol.

Formation of Active FA—NHS Ester and Coupling To Form NH$_2$—SiO$_2$@Fe$_3$O$_4$ Conjugates. A 250 mg (0.28 mmol, 1 equiv) portion of folic acid was dissolved in 5 mL of DMSO. To this solution was added 114 mg (0.28 mmol, 1 equiv) of DCC, and the reaction mixture was stirred for 3 h. Afterward, 64 mg (0.28 mmol, 1 equiv) of NHS was added and the solution was aged for 24 h. To immobilize folic acid on the Fe$_3$O$_4$—SiO$_2$—NH$_2$ nanoparticles, the generated dicyclohexylthiourea was filtered off under inert conditions and the filtrate was added to a three-necked flask equipped with a mechanical stirrer. The vacuum-dried Fe$_3$O$_4$—SiO$_2$—NH$_2$ nanoparticles were dissolved by sonification in 5 mL of dry DMSO and added to the activated folic acid solution. The whole solution was stirred for 24 h and the Fe$_3$O$_4$—SiO$_2$—NH—FA nanoparticles were removed and washed several times with PBS by magnetic attraction.

Characterization. The morphology and size of as-prepared products were observed by transmission electron microscopy (TEM) using a JEOL 2100 HR-(S) TEM instrument with a LaB$_6$ electron source operating at 200 kV. For scanning electron microscopy (SEM) measurements, a FEI Quanta 50 FEG Series microscope fitted with an Oxford INCA EDS detector was used. Ultraviolet—visible (UV—vis) spectra were obtained using a CARY 50 Scan UV—visible spectrometer. Fourier-transform infrared (FTIR) spectroscopy measurements were recorded on a PerkinElmer FTIR spectrophotometer. The X-ray diffraction (XRD) analysis was carried out on a Philips X'Pert diffractometer using Cu Kα radiation (λ = 1.504 nm). A scan rate of 0.05°/s was applied to record the pattern in the 2θ range of 10°—80°. The Mössbauer spectra measurements were done in the transmission mode with ^{57}Co diffused into Rh matrix as the source moving with constant acceleration (Wissel-MA 260S). The spectrometer was calibrated by means of a standard α—Fe foil and the isomer shift was expressed with respect to this standard at 293 K. The samples were measured at the temperature of 293 K. A LND-45431 proportional counter distributed by Wissel GmbH was used for recording the spectra. The data were analyzed with Lorentzian sextets (Software NORMOS). Magnetic measurements were performed with a superconducting quantum interference device (SQUID) magnetometer (Quantum Design, MPMS XL-7). Microanalysis for C, H, N, and S was carried out using a Hekatech CHNS EuroEA 30000 analyzer with helium as carrier gas. Thermogravimetric analysis (TGA) were performed on a TGA/DSC 1 STAR^e system by Mettler with a GC 100 gas controller in a flowing nitrogen atmosphere employing a heating rate of 10 °C/min. The IR measurements were carried out on a FTS 3000 instrument from Bio-Rad. The dynamic light scattering experiments (DLS) and measurement of ζ-potential were performed with a Malvern instruments Zetasizer Nano SZ. Nuclear magnetic resonance (NMR) spectra were recorded with a Bruker AVANCE II 300 spectrometer at 298 K. The Brunauer—Emmett—Teller (BET) surface of the samples was determined from nitrogen sorption measurements using a Belsorp Mini II apparatus from BEL. X-ray photoelectron spectroscopy (XPS) measurements were carried out on a Surface Science Instruments SSX-101 ESCA M-Probe system using monochromatic Al Kα radiation (1486.6 eV).

Cytotoxicity Assay via MTT. Two different cell types were used for the in vitro study of the nanostructure cytotoxicity: L929 mouse fibroblast cells and HEK 293.

For the MTT assay, 2 mg of dried nanoparticles were dispersed in 2 mL of sterile water and exposed to UV light overnight. The nanoparticle solutions were dispersed in cell culture medium (DMEM) to obtain the following concentrations: 5, 10, 20, 50, and 100 μg/mL. For performing the MTT assay, 150 μL of dispersed cells (7.5 × 10^4 cells/mL) was placed in each well of a 96-well plate (Greiner GmbH) and incubated for 24 h at 37 °C and 5% CO$_2$. The supernatant medium was carefully removed, and 200 μL of nanoparticle solution with the desired concentration was added, and the mixture incubated for 24 and 48 h, respectively. For the positive

Scheme 1. Schematic Outline of the Synthetic Pathway for FA@SiO₂@Fe₃O₄ Nanoparticles[a]
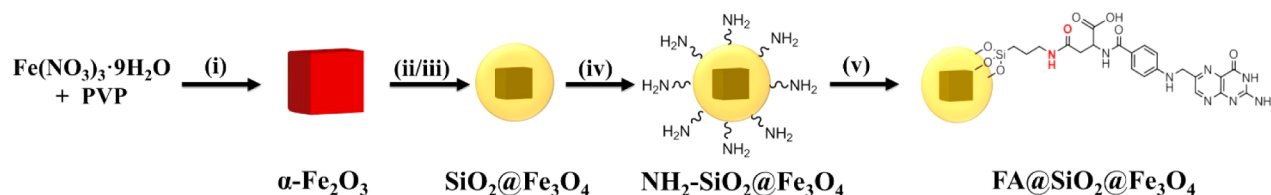
^{a}α-Fe$_2$O$_3$ quasicubic particles were synthesized by a facile solvothermal process (i), followed by the silica shell formation with TEOS (ii) and the core reduction to magnetite (iii). The surface of the SiO$_2$@Fe$_3$O$_4$ nanoparticles was activated with amine groups (iv) and vectorized by covalent attachment of FA as the targeting unit (v).
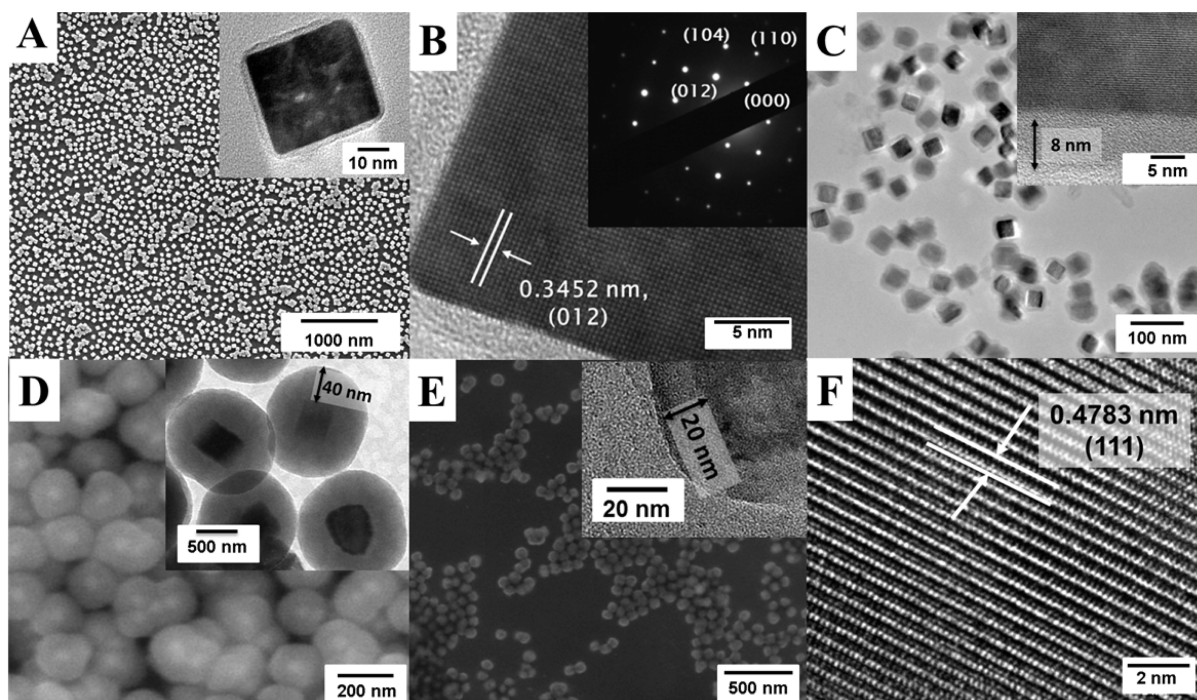
Figure 1. Panels A and B show the SEM and HR-TEM analysis of α-Fe$_2$O$_3$ nanoparticles. The modified SiO$_2$@Fe$_2$O$_3$ nanoparticles with a shell thickness of 8 and 40 nm are shown in panels C and D, respectively. Exemplary SiO$_2$@Fe$_3$O$_4$ nanoparticles with a shell thickness of 20 nm are shown in panel E. The HR-TEM of the Fe$_3$O$_4$ core is highlighted in panel F. All insets show the depicted nanoparticles with higher resolutions.

control, the cells were grown without exposure to the nanoparticle solution. After the desired incubation time the supernatant was removed and 40 μL of MTT solution (5 mg in 1 mL of PBS) was added. Subsequently, after 2 h of incubation, 150 μL of DMSO was added and the absorption (490 nm with a reference of 630 nm) was measured using a Elisa plate reader. Afterward, the absorption values were assessed relative to the absorption values from the cells in the control experiment.

Interference Studies. In order to exclude any interference of the MTT assay with the nanoparticles, 150 μL of medium was incubated with nanoparticles at different concentrations (5, 10, 20, 50, and 100 μg/mL) and 40 μL of MTT for 2 h. Afterward, 150 μL of DMSO was added and the absorption (490 nm with a reference of 630 nm) was evaluated using the Elisa plate reader.

RESULTS AND DISCUSSION

The typical synthetic steps required for obtaining FA@SiO$_2$@Fe$_3$O$_4$ hybrid nanoparticles involved (i) solvothermal synthesis of cube-shaped α-Fe$_2$O$_3$ particles, (ii) silica-coating by condensation of silicic acid on α-Fe$_2$O$_3$ particles and modulation of the thickness of silica over layer by subsequent and sequential condensation of TEOS, (iii) reduction of hematite core to form magnetite, (v) grafting of terminal

surface groups by condensation of siloxane coupling reagent (3-aminopropyl)trimethoxysilane, and (vi) covalent attachment of folic acid on the amine-terminated surface groups (Scheme 1).

Preparation of SiO$_2$@Fe$_2$O$_3$ Nanocomposites. α-Fe$_2$O$_3$ nanoparticles were synthesized similar to the solvothermal procedure described by Zheng et al.[41] The X-ray diffraction pattern of the as-prepared particles (Figure 2D) displayed the diffraction peaks corresponding to the hematite phase with the trigonal space group R3c ($a = b$ = 0.503 nm and c = 1.373 nm; $\alpha = \beta$ = 90° and γ = 120°; PDF no. 13-0534). This is in variance to the space group reported by Zheng et al. for quasicubic α-Fe$_2$O$_3$ and probably caused by the varied chain length of PVP as well as the reaction volume in the Teflon inlet and therefore changed pressure. The average crystallite size ($\langle d \rangle$) was estimated to be ca. 35 nm using the Debye–Scherrer equation[42] $D = K\lambda/\beta \cos \Theta$ (where K is the Scherrer constant, λ is the X-ray wavelength, β is the peak width of half-maximum, and Θ is the Bragg diffraction angle). The average grain size was found to be in good agreement with the particle size determined by SEM and HR-TEM analyses (Figure 1) that verified the particles to be single-domain and possess a narrow size-dispersion. The morphology and geometrical shape of the
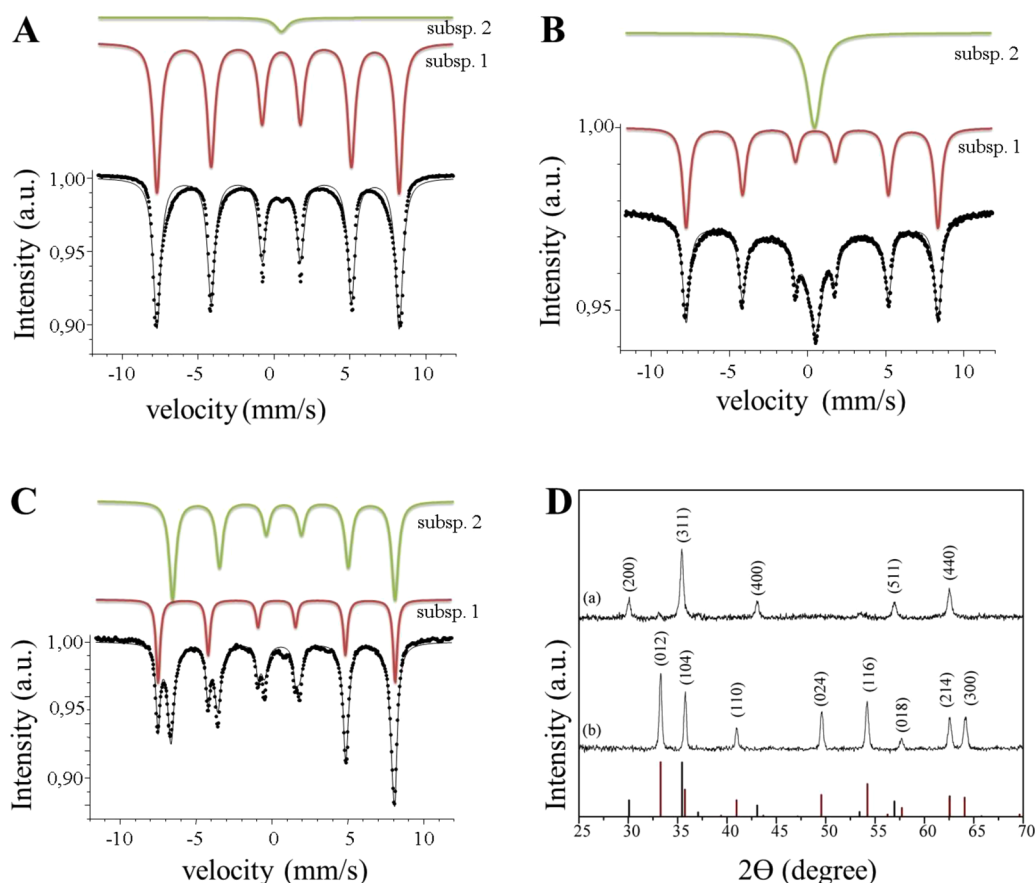
Figure 2. (A) Mössbauer spectra of as-prepared Fe_2O_3 nanocubes, (B) SiO_2@Fe_2O_3 nanocomposites coated with a 20 nm SiO_2 shell, and (C) reduced SiO_2@Fe_3O_4 nanocomposites. Each sample was measured at room temperature and fitted with NORMOS. (D) XRD pattern of SiO_2@ Fe_2O_3 before (b) and after reduction (a) under Ar/H_2 (95:5 vol %) for 4 h at 350 °C displaying a transition from hematite (PDF no. 13-0534, red) to magnetite (PDF no. 85-1436, black).

particles were influenced by small amounts of PVP that were found to be present at the surface even after several washing steps, making them stable in water and ethanol. The presence of the smooth organic layer of approximately 2 nm thickness on the particle surface became visible in the HR-TEM analysis (inset, Figure 1A) due to significant differences in the image contrast between organic and inorganic phases. Further TGA and FT-IR analysis confirmed the presence of the PVP linker (Figures S1 and S2, Supporting Information. The DLS measurement of α-Fe_2O_3 nanoparticles revealed a hydrodynamic radius of 89.2 nm in water with a polydispersity index (PDI) of 0.205, displaying a good dispersibility (Figure S3, Supporting Information), which was essential for the following steps leading to silica shell formation.

For the coating process, a primer layer of silicic acid was introduced on the nanoparticle surface (Scheme 1) that acted as a surface-anchored seed layer for further growth of the silica shell by condensation of TEOS.[43] The shell thickness could be tuned between 8 and 40 nm (Figure 1C-E) by varying the amounts and addition steps of TEOS. Exemplarily, SiO_2@ Fe_2O_3 nanocomposites are shown in Figure 1C,D with clear evidence for distinct composition of core and shell materials. Interestingly, the thinner (<5 nm) silica layer followed the core morphology and formed cube-shaped composited nanoparticles, whereas in the case of higher shell thickness (>20 nm), the morphology of the nanocomposites became almost spherical (Figure S4, Supporting Information), which was more

prominent when the shell thickness was extended to 40 nm (Figure 1D,E). This is evidently due to surface energy considerations, which achieves a minimum for the spherical form. Furthermore, the morphology of the particles was found to be maintained after the chemical modification with the silanation agent, indicating that further surface activation/ vectorization would not change the particle morphology.

Conversion of SiO_2@Fe_2O_3 Structures to SiO_2@Fe_3O_4 Nanoparticles. To enhance the magnetic properties of the nanovector, the α-Fe_2O_3 cores were reduced to magnetite by treating them in a forming gas atmosphere to obtain superparamagnetic SiO_2@Fe_3O_4 nanoparticles. The controlled reductive atmosphere and mild processing conditions enabled the retention of the cube-shaped morphology, as can be seen in the TEM analysis (Figure 1E). To underline the necessity of this multistep coating process, the bare α-Fe_2O_3 nanoparticles were reduced to Fe_3O_4, and a subsequent coating process following the same synthetic procedure was performed. The yielded particles showed formation of clustered nanoparticles, which were not stable in aqueous solution (Figure S5, Supporting Information) as the coating process was hindered due to the high magnetic moment of Fe_3O_4 nanoparticles (Figure 6A).

The complete conversion of the hematite phase into pure magnetite by the chosen conditions for SiO_2@Fe_3O_4 nanoparticles was proven by XRD (Figure 2D). The diffraction peaks corresponded to the magnetite phase with the cubic

space group $Fd\bar{3}m$ ($a = b = c = 0.839$ nm; $\alpha = \beta = \gamma = 90°$; PDF no. 85-1436). The forming gas (mixture of hydrogen and nitrogen) treatment had a direct control on the particle surface, and the reduction time was found to be crucial for controlling the composition as prolonged reductive treatment led to the formation of metallic iron (Figure S6, Supporting Information).[44]

The phase transformation from $SiO_2@Fe_2O_3$ to $SiO_2@Fe_3O_4$ was also monitored by Mössbauer spectroscopy to analyze the phase purity of the iron oxide core and to exclude the possible coexistence of other phases, such as metallic iron or maghemite (γ-Fe_2O_3), that can form during the forming gas treatment (Figure 2 and Table S1, Supporting Information). The Mössbauer spectroscopy data recorded at room temperature and fitted with the help of the NORMOS program are summarized in Table S1 (Supporting Information). The Mössbauer spectra of untreated samples (as-prepared α-Fe_2O_3 nanocubes) revealed one independent sextet with isomer shift and quadruple splitting values corresponding to the published values (Figure 2A).[45] The hyperfine field value was found to be smaller than the reported one (51.7 T), which is possibly caused by the decrease of B_{Hf} with decreasing particle size. The broad singlet, which could be fitted in subspectrum 2, corresponded to Fe^{3+} ions present on the nanoparticle surface in the paramagnetic state. After the completion of the coating process with silica, the area of the singlet increased from 3% to 32% in relation to the area of the Fe^{3+} in subspectrum 1 corresponding to the hematite phase (Figure 2B). This broad singlet could be assigned to a collapsed doublet or sextet caused by Fe^{3+} ions in the paramagnetic or superparamagnetic state. The increased amount of free ions could be caused by the coating process as in the water glass process, performed under acidic conditions, where the surface ions can leach out and get incorporated in the silica matrix.[46] After the reduction with the forming gas no free ions were visible in the spectra anymore, which reinforced a complete transformation of a distinct iron oxide phase. The spectrum of $SiO_2@Fe_3O_4$ was fitted by two independent sextets, which corresponded to a magnetically ordered phase (Figure 2C). The subspectrum 1 revealed the Fe^{3+} ions in the tetrahedral positions, whereas subspectrum 2 corresponded to the Fe^{3+} and Fe^{2+} ions in the octahedral positions. The parameters of the subspectrum fitted well with the parameters of magnetite reported in the literature.[45] The ratio of iron in the tetrahedral position to iron in the octahedral position calculated from the area of sextets is equal to 1:2, displaying reasonable stoichiometry of the magnetite core and evidence for a complete conversion.

The SEM image of cube-shaped Fe_3O_4 nanoparticles (Figure S7, Supporting Information) reduced without a protective silica shell showed a perfect alignment along the magnetic field lines of an external magnetic field, indicating their stronger magnetization behavior. SEM and HR-TEM of $SiO_2@Fe_3O_4$ nanoparticles are shown in Figure 1E,F, which confirmed the single-domain character of the nanoparticles and a uniform shell formation. The HR-TEM image of the reduced $SiO_2@Fe_3O_4$ showed (Figure 1F) lattice planes with a distance of 0.4783 nm assignable to the (111) plane of the magnetite phase. Although no obvious change in the particle morphology after core reduction was detected by HR-TEM analysis (Figure 1C,E), nitrogen absorption/desorption measurements were performed to get a better insight whether any change in surface area and porosity can be observed. Figure 3 shows the adsorption/desorption isotherms of the samples before (red)
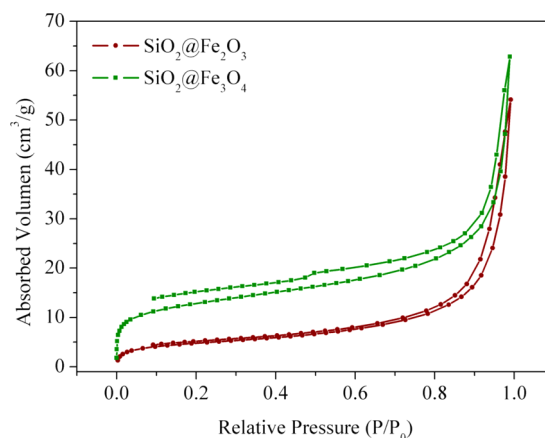
Figure 3. Absorption−desorption plots of the nanoprobes before and after the core reduction of $SiO_2@Fe_2O_3$ (red) and $SiO_2@Fe_3O_4$ (green).

and after (green) the reduction. For both samples the isotherms were classified as type IV isotherms.[47] The almost negligible hysteresis loop between adsorption and desorption processes in both samples suggested the formation of a monolayer of N_2 molecules on the inner wall of the pores.[48] The adsorption loop at $P/P_0 \sim 0.95$ was attributed to macropores formed by interparticle voids formed among the nanoparticles upon drying. The surface area of unreduced $SiO_2@Fe_2O_3$ nanoparticles was estimated by BET to be 17.5 m^2/g and it was found to increase to 45 m^2/g after the reduction process, probably due to the possible perforation of the silica shell, which is necessary for the inward diffusion of forming gas to reduce Fe^{3+} to Fe^{2+} and for the outward diffusion of gaseous species formed in the reduction process (O_2 or H_2O). This was clearly visible in the $SiO_2@Fe_3O_4$ isotherms observed in the relatively low relative pressure ($P/P_0 = 0-0.1$) regime. The results indicated the formation of small pores with around 2 nm diameter with an area of 21 m^2/g as this increase was caused by the capillary condensation of nitrogen within these pores. The increased surface area and formation of pores after the reduction process is advantageous for the following surface modification as the enhanced surface area provided more space for the organic vectors (vide infra).

Surface Activation and Vectorization of $SiO_2@Fe_3O_4$ with −NH_2 Group and FA Attachment. For targeted attachment of folic acid, the $SiO_2@Fe_3O_4$ nanoparticles were functionalized with an amine linker. For this purpose, APTMS was used as a primer followed by the covalent-binding of FA on the nanoparticle surface via an activated ester route (Scheme 1). Since folic acid has two carboxylic groups, the selective activation of only one carboxylic group is challenging.[49,50] Therefore, FA was first allowed to completely dissolve before the coupling reagents dicyclohexylcarbodiimide (DCC) and N-hydroxysuccinimide (NHS) were added to the reaction solution. The reaction was implemented in DMSO as folic acid exhibits poor solubility in most of the common organic solvents. First, DCC was added to the solution to form the amine-reactive O-acylisourea ester; since it is an unstable intermediate and susceptible for hydrolysis, NHS was added to stabilize the amine-reactive ester. In this process, dicyclohexylthiourea is formed as a side product, which is removed via inert filtration. The filtrate containing the active FA−NHS intermediate was directly coupled to the nanoparticle surface by addition to a previously prepared NH_2−$SiO_2@Fe_3O_4$ suspen-
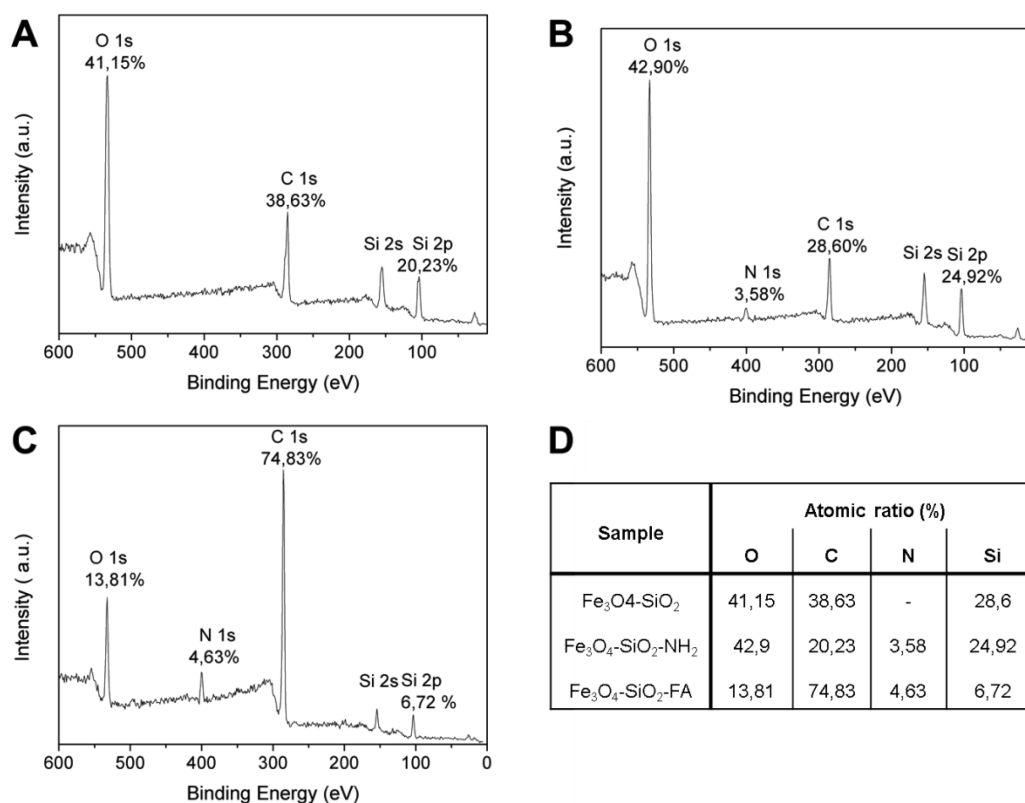
Figure 4. XPS spectra of $SiO_2@Fe_3O_4$ (A), $NH_2-SiO_2@Fe_3O_4$ (B), and $FA@SiO_2@Fe_3O_4$ (C). The elemental ratios in atomic weight percent of the three compounds are summarized in part D.

sion. To prevent particle agglomeration, excess of FA was removed via several washing steps with PBS by magnetic agitation until the supernatant did not show any color change. Following this synthetic procedure, almost quantitative coupling was obtained as verified by EA, TGA, XPS, and AT-IR analyses.

FA−NHS was precipitated in an acetone/ether mixture and dried under vacuum. The AT-IR spectra of FA−NHS did not show the distinct −OH stretching vibrations present in free folic acid at 3542, 3419, and 3319 cm^{-1}, which suggested the covalent bonding of FA (Figure S8A,Supporting Information). Moreover, a new broad absorption band in the region from 3500 to 3000 cm^{-1} was observed indicative of the successful FA−NHS synthesis. The successful formation of the reactive FA−NHS species was further confirmed by NMR and EA (Figure S8B, Supporting Information).

XPS Analysis. XPS wide-scan spectra were performed after each step of surface functionalization to map the surface chemistry of the nanoprobes (Figure 4). The distinctive peaks of Fe, which were expected at 56 eV Fe 3p and 712 eV Fe 2p,[51,52] are not visible in the XPS spectra, as XPS is a surface-sensitive probe (analytical depth of a few nanometers), which indicated the complete coverage of FeO_x particles with a silica shell. Furthermore, the successful surface functionalization with amino groups by condensation of the APTMS primer toward the silanol groups on the particle surface was validated by the appearance of the 1s N signal at 400 eV in the coated nanoparticles (Figure 4B). The attachment of FA on the $NH_2-SiO_2@Fe_3O_4$ nanoparticles was also observed in the XPS spectra (Figure 4C). Due to the fact that there are seven nitrogen atoms with different electronic surroundings in the folic acid molecule, a conclusive identification of the newly

formed amide bond was not possible; however, the change in the atomic ratio of the different atoms on the particle surface was distinct (Figure 4D).

Thermogravimetric and Elemental Analysis. Further evidence of the changed surface chemistry was given by TGA analyses (Figure 5A). Whereas bare $SiO_2@Fe_3O_4$ nanoparticles did not show any weight loss before 350 °C, the increased weight loss of about 12.5 wt % after the NH_2 functionalization was indicative of the decomposition of the aminopropyl chain and proved the successful attachment of the primer molecules. After the covalent attachment of folic acid, an increased weight loss of 38 wt % was observed, which was apparently caused by the decomposition of both aminopropyl groups and folic acid. Following the estimation made by Huang et al.,[49] which assumed a 1:1 ratio of amine linker and folic acid, our particles should contain approximately 25.5 wt % of folic acid. By taking into account the molar mass of each compound, the ratio of primer to folic acid can be estimated to be 1:1, indicating a successful covalent attachment and complete utilization of the amine primer.

The chemical composition of the organic part of the nanoparticle conjugates was estimated by elemental analysis of the particles (Figure 5D). The organic fraction determined by elemental analysis for all the samples was found to be lower than that determined by TGA. This might be caused by the different nature of the experimental setup. Nevertheless, $NH_2-SiO_2@Fe_3O_4$ nanocomposites showed an amine content of 0.51%, in contrast to unmodified $SiO_2@Fe_3O_4$ nanoparticles, where no amine could be detected. This is in accordance with the presence of the amine linker. Once folic acid is coupled, the nitrogen, carbon, and hydrogen amounts increased, which is in
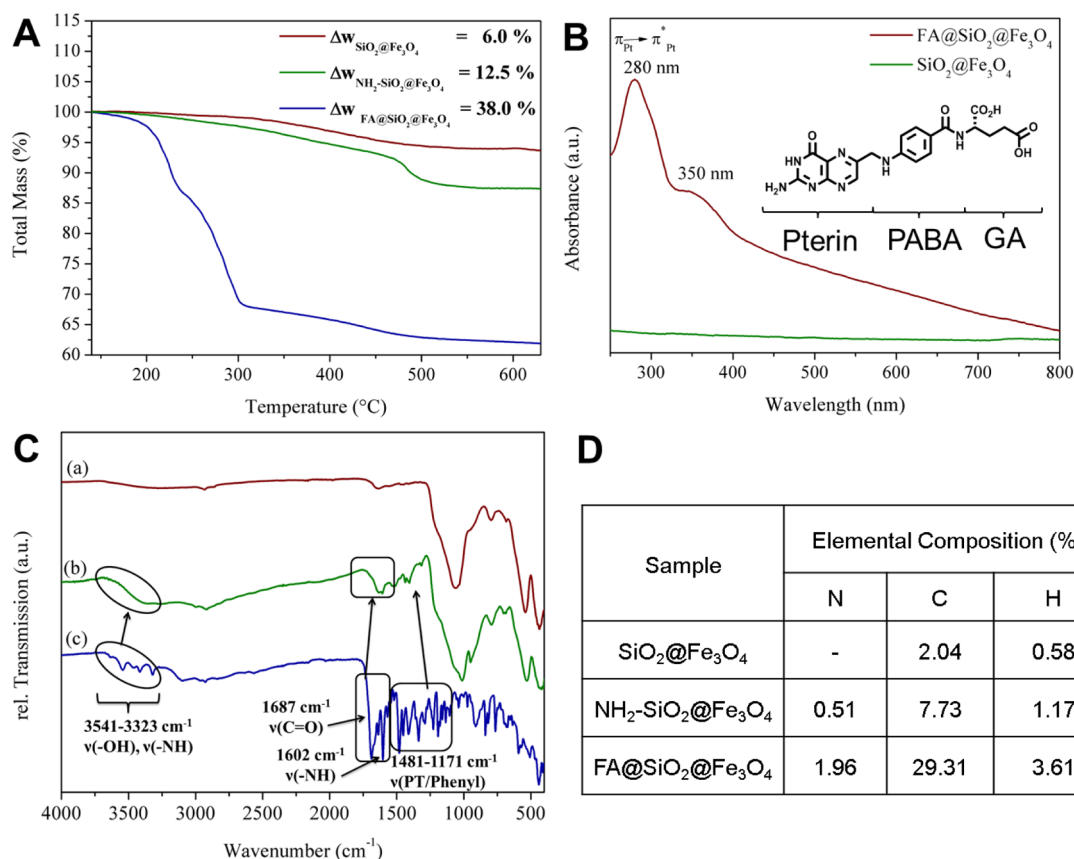
Figure 5. TGA of $SiO_2@Fe_3O_4$, $NH_2-SiO_2@Fe_3O_4$, and $FA@SiO_2@Fe_3O_4$ revealing the enhanced organic content after each step of surface functionalization (A). UV−vis of $SiO_2@Fe_3O_4$ and $FA@SiO_2@Fe_3O_4$ measured in PBS-buffer solution (B). AT-IR spectra of $SiO_2@Fe_3O_4$ (a, red), $FA@SiO_2@Fe_3O_4$ (b, green), and pure folic acid (c, blue) (C). Summary of the elemental analysis performed after each functionalization step (D).

good agreement with the presence of the targeting unit as an integral part of the functionalized nanoparticles.

Qualitative Analysis of Surface Modification. The AT-IR spectra of unmodified $SiO_2@Fe_3O_4$ and modified $H_2N-SiO_2@Fe_3O_4$ nanoparticles (Figure S10, Supporting Information) showed a very broad band with low intensity around 3350 cm^{-1}, corresponding to surface silanol groups and water molecules absorbed by the porous surface. The successful coating with the silica shell was further approved by the band around 1054 cm^{-1}, corresponding to Si−O−Si cm^{-1} stretching vibrations as well as the bands at 935 and 796 cm^{-1} that represented surface silanol groups.[53] The Fe−O stretching vibrations at 550 and 441 cm^{-1} were present in each of the spectra and clearly corresponded to the presence of the FeO_x core. Also, the CH_2 stretching vibrations were attributed to the propyl chain of APTMS, which were visible at 2958, 2920, and 2853 cm^{-1} (Figure S10B, Supporting Information). The observation of methoxy vibrations at 1211 and 1152 cm^{-1} on the other hand suggest an incomplete condensation of APTMS. Upon prolonging the reaction time, the AT-IR spectra did not show methoxy peaks anymore, leading to the conclusion that APMTS was successfully condensed on the surface (Figure S10C, Supporting Information). Weak peaks around 1460 cm^{-1} are visible in both spectra, which prolonged the N−H stretching vibrations, corroborating the presence of $-NH_2$ groups on the surface.

Figure 5C shows the AT-IR analysis of $SiO_2@Fe_3O_4$, $FA@SiO_2@Fe_3O_4$, and pure FA that contains the fingerprint absorption and other characteristic vibrations of the hetero-

cyclic pterin ring (PT), p-aminobenzoic acid (PABA), and glutamic acid (GA) from which folic acid is composed. The stretching vibrations of −OH and −NH exhibited a finely split band before the attachment that was noted after covalent bonding as a broad peak around 3541−3323 cm^{-1}. Furthermore, the stretching vibrations of the carbonyl and amine groups were visible at 1687 and 1602 cm^{-1}, respectively, and found to be slightly shifted after the attachment to lower wave numbers resulting from the differing electronic surrounding. The stretching vibrations of the pterin and phenyl ring were also visible after the attachment between 1481 and 1171 cm^{-1} as well as the Si−O−Si and Fe−O stretching vibrations corresponding to the nanoparticle core.

The UV−vis absorption spectra of $SiO_2@Fe_3O_4$ and $FA@SiO_2@Fe_3O_4$ measured in PBS buffer solution (Figure 5B) showed a distinct absorption peak at 280 nm corresponding to the $\pi \rightarrow \pi^*$ transition of the pterin ring[54,55] and a broad shoulder around 350 nm, whereas a broad absorption in the UV−vis region was observed in the unmodified $Fe_3O_4-SiO_2$. After folic acid coupling, the bands at 280 and 350 nm were clearly visible in the spectra, which validated the successful attachment of folic acid units.

ζ-Potential Measurements. For cellular uptake of nanoparticles, surface charge and colloidal stability are the crucial factors.[56] It has been shown that positively charged nanoparticles are prevalently taken up by cancer cells.[57] However, it has been also shown that folic acid-targeted nanoparticles are actively internalized by cancer cells, despite their high negative ζ-potential.[11,58] To better understand the colloidal behavior of
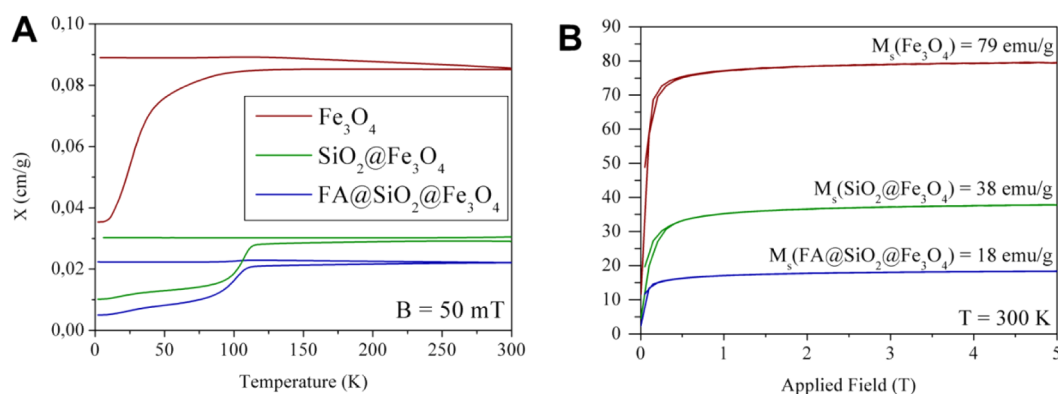
Figure 6. Magnetization measurements of the nanoparticles after each step of functionalization at room temperature (A). FC and ZFC curves of all samples measured at an applied field of 50 mT (B).
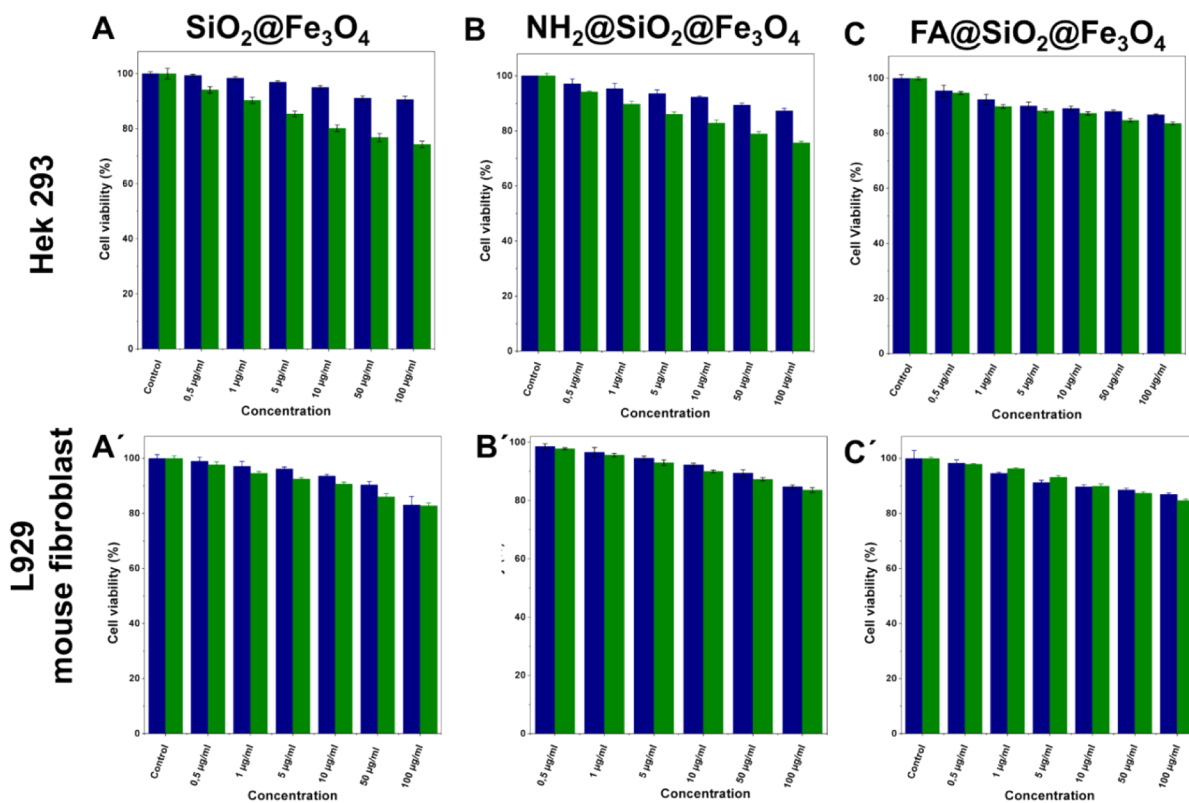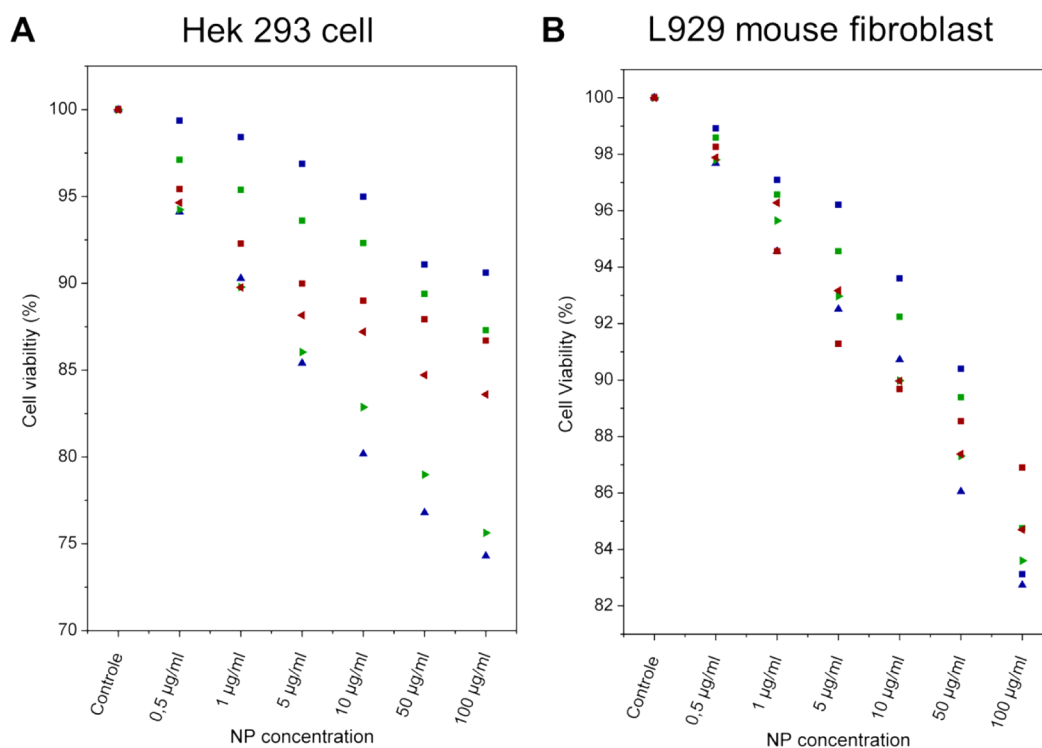

Figure 7. Cell viability tests of Hek 293 cells (A−C) and L929 mouse fibroblast (A′−C′) exposed to $SiO_2@Fe_3O_4$ (A, A′), $NH_2−SiO_2@Fe_3O_4$ (B, B′), and $FA@SiO_2@Fe_3O_4$ (C, C′) nanoparticles. Blue bars are measured after 24 h and green bars after 48 h of incubation.

our system, ζ-potential measurements of each sample ($SiO_2@Fe_3O_4$, $H_2N-SiO_2@Fe_3O_4$, $FA@SiO_2@Fe_3O_4$) were performed at pH 7 (Figure S11, Supporting Information). The ζ-potential of $SiO_2@Fe_3O_4$ was found to be −32.9 mV, due to the −OH groups on the surface. This high value also revealed the good colloidal stability of the particles, which was of crucial importance for the following functionalization process. The ζ-potential shifted to +32.2 mV, caused by the −NH_2 groups present on the surface. The huge shift in the value also indicated the successful coating and good coverage of the surface. After the covalent attachment of folic acid, the value shifted to −20.0 mV, suggesting that the good colloidal stability of the particles was maintained after functionalization, which is an essential prerequisite for cell tests.

Magnetic Measurements. The magnetic behavior of the nanoparticles was investigated using a superconducting quantum interference device, SQUID MPMS-XL, from Quantum Design. For α-Fe_2O_3 nanocubes the magnetic saturation was not achieved until the maximum applied field of 4 T (Figure S12, Supporting Information). The maximum magnetization was 0.87 emu/g. This is in good agreement with values reported for hematite nanoparticles in the literature.[59] As expected, the saturation magnetization increased after the conversion to 79 emu/g for Fe_3O_4 (Figure 6A). The latter was slightly lower than the expected value for the bulk material [M_s(bulk) = 92 emu/g].[60] Both compounds showed superparamagnetic behavior due to their relatively small crystal sizes and canted antiferro- or ferrimagnetic nature, respectively. After coating the Fe_3O_4 nanoparticles with silica, the saturation magnetization decreased to 38 emu/g, caused by the mass dilution by the coating material (diamagnetic SiO_2). Hence, the mass ratio of Fe_3O_4 to SiO_2 was approximately 1:1,

Figure 8. Comparison of the cell viability of Hek 293 cells (A) and L929 mouse fibroblast (B) exposed to $SiO_2@Fe_3O_4$, $NH_2-SiO_2@Fe_3O_4$, and $FA@SiO_2@Fe_3O_4$ nanoparticles. The square symbols indicate cell viabilities measured after 24 h and the triangle symbols after 48 h of incubation. $SiO_2@Fe_3O_4$ nanoparticles are shown in blue, $NH_2-SiO_2@Fe_3O_4$ in green, and $FA@SiO_2@Fe_3O_4$ in red.

corresponding to a molar ratio of roughly 1:4. After the functionalization with FA, the magnetization per mass was further reduced to 18 emu/g. This was possibly a consequence of the surface functionality, which further lowers the mass ratio of magnetic material. Using the same simple considerations, the mass ratio would then be close to 1:1:2 (Fe_3O_4:SiO_2:FA), which was slightly higher than the mass ratio obtained by TGA (1:1:1.4). This direct relation to the mass is possible due to the fact that the diamagnetic signal from the nanoparticle coating is negligible in comparison to that of the magnetite particle. With a significantly thicker coating this direct assumption is no longer valid.

The coating also affected the difference between ZFC and FC curves (Figure 6B). For the bare Fe_3O_4 nanoparticles a broad drop in the ZFC was observed, leading to the assumption of two blocking temperatures at 30 and 90 K. This could be explained by the presence of particle aggregates with slightly varying sizes, causing a range of magnetic interparticle interaction strengths. The silica-coated particles exhibited a more well-defined blocking temperature that progress in a single step. This indicated that the particle aggregation is reduced as the superparamagnetic domain size is homogeneous. Therefore, the $SiO_2@Fe_3O_4$ nanoparticles show one relatively sharp blocking temperature at 115 K. After the FA attachment, the ZFC and FC curves mostly remained the same. Just a slight decrease in the blocking temperature to 109 K was observed, which might correlate with the expected larger average distance between the magnetic particles. The magnetic nature and redispersible nature of $SiO_2@Fe_3O_4$ nanocomposites were also visualized in Figure S13 (Supporting Information).

Cytotoxicity Assessment. Recent reports by various groups have shown that the immune response of cells toward foreign matter such as nano- or microparticles highly depends

on the chemical composition and surface chemistry.[61−64] In order to test the biocompatibility and possible applicability of these particles for MRI imaging, cell viability tests were performed for nontargeted $SiO_2@Fe_3O_4$, $NH_2-SiO_2@Fe_3O_4$, and targeted $FA@SiO_2@Fe_3O_4$ nanovectors. Before the particles were tested in the cells, interference studies were performed to exclude any interaction between the in situ formed formazan and the nanoparticles, which could lead to an enhanced absorbance and therefore false interpretation of our results.[65−67] The measured absorbance was so low that any viable interaction could be excluded. After incubation of Hek 293 and mouse fibroblast cells L929 for 24 and 48 h at particle concentrations of 0.5, 1, 5, 10, 50, and 100 μg/mL, MTT assay was used to evaluate the cell viability (Figure 7). It was found that that cell viability of mouse fibroblast cells did not show significant decrease for each kind of particle after 24 and 48 h (Figure 8). Nevertheless, a slight decrease in cell viability was observed at higher concentrations (100 μg/mL). In the context of the Hek 293 cells, the cell viability decreased for cells exposed to $SiO_2@Fe_3O_4$ and $NH_2-SiO_2@Fe_3O_4$ after 48 h. The result of cell assays confirmed that the vectorized particles are not significantly cytotoxic, even at very high concentrations of 100 μg/mL

■ CONCLUSION

Development of ultrasmall multimodal probes, unifying therapeutic and diagnostic functions, using biologically benign nanoparticles and their conjugation with appropriate vectors carries unfolding promise for pharmaceutical nanotechnology. Herein, $FA@SiO_2@Fe_3O_4$ nanocomposites were successfully prepared starting from highly colloidal stable α-Fe_2O_3 nanocubes coated with conformal silica shell of tunable thickness. The demonstrated precise coating procedures allowed the

retention of the core size and shape as well as well as imparted colloidal stability in aqueous medium to core−shell nanostructures. The strategy of preparing bioconjugated magnetic probes by ex situ reduction of weakly ferromagnetic α-Fe$_2$O$_3$ phase allowed the formation of monodisperse nanoparticles by suppressing the magnetic interaction during the shell formation. Comprehensive analytical investigations by Mössbauer spectroscopy, XRD, and magnetization data confirmed the reduction (hematite → magnetite) of core particle under conservation of cube-shaped morphology. The successful vectorization of SiO$_2$@Fe$_3$O$_4$ nanoprobes with the cell-targeting unit folic acid was demonstrated by several quantitative and qualitative analytical studies. The cytotoxicity studies revealed the biocompatible nature of the nanoprobes, making the bioconjugated nanoprobes a promising tool for MRI.

■ ASSOCIATED CONTENT

Ⓢ Supporting Information

The DLS, FT-IR, TGA, and SQUID measurements of as-prepared α-Fe$_2$O$_3$ nanoparticles, ζ-potential measurements, additional SEM images, and XRD studies are provided, as well as NMR, elemental analysis, TGA, and FT-IR analysis of FA−NHS. This material is available free of charge via the Internet at http://pubs.acs.org.

■ AUTHOR INFORMATION

Corresponding Author

*E-mail: sanjay.mathur@uni-koeln.de. Tel: +49 221 470 5627. Fax: +49 221 470 4899.

Notes

The authors declare no competing financial interest.

■ ACKNOWLEDGMENTS

■ REFERENCES

(1) Chaudhuri, R. G.; Paria, S. Core/Shell Nanoparticles: Classes, Properties Synthesis Mechanisms, Characterization, and Application. *Chem. Rev.* **2012**, *112*, 2373−2433.

(2) Song, Q.; Zhang, Z. J. Controlled Synthesis and Magnetic Properties of Bimagnetic Spinel Ferrite CoFe$_2$O$_4$ and MnFe$_2$O$_4$ Nanocrystals with Core−Shell Architecture. *J. Am. Chem. Soc.* **2012**, *134*, 10182−10190.

(3) Zhang, J.; Liu, X.; Wang, L.; Yang, T.; Guo, X.; Wu, S.; Wang, S.; Zhang, S. Au-Functionalized Hematite Hybrid Nanospindles: General Synthesis, Gas Sensing and Catalytic Properties *J. Phys. Chem. C* **2011**, *115*, 5352−5357.

(4) Maleki, M.; Amani-Tehran, M.; Latifi, M.; Mathur, S. Drug Release Profile in Core-Shell Nanofibrous Structures: A Study on Peppas Equation and Artificial Neural Network Modeling. *Comput. Methods Programs Biomed.* **2014**, *113*, 92−100.

(5) Rizzo, L. Y.; Theek, B.; Storm, G.; Kiesling, F.; Lammers, T. Recent Progress in Nanomedicine: Therapeutic, Diagnostic and Theranostic Application. *Curr. Opin. Biotechnol.* **2013**, *24*, 1159−1166.

(6) Kumar, S.; Jana, A. K.; Maiti, M.; Dhamija, I. Carbodiimide-Mediated Immobilization of Serratiopeptidase on Amino-, Carboxyl-Functionalized Magnetic Nanoparticles and Characterization for Target Delivery. *J. Nanopart. Res.* **2014**, *16*, 2233.

(7) Ren, Y.; Abbood, H. A.; Fengbo, H.; Peng, H.; Huang, K. Magnetic EDTA-Modified Chitosan/SiO$_2$/Fe$_3$O$_4$ Adsorbent: Preparation, Characterization, and Application in Heavy Metal Adsorption. *Chem. Eng. J.* **2013**, *266*, 300−311.

(8) Kralij, S.; Rojnik, M.; Kos, J.; Makovec, D. Targeting EGFR-Overexpressed A431 Cells with EGF-Labeled Silica-Coated Magnetic Nanoparticles. *J. Nanopart. Res.* **2013**, *15*, 1666.

(9) Ilyas, S.; Ilyas, M.; van der Hoorn, R. A. L.; Mathur, S. Selective Conjugation of Proteins by Mining Active Proteomes through Click-Functionalized Magnetic Nanoparticles. *ACS Nano* **2013**, *7*, 9655−9663.

(10) Li, N.; Binder, W. H. Click-Chemistry for Nanoparticle Modification. *J. Mater. Chem.* **2011**, *21*, 16717−16734.

(11) Das, M.; Bandyopadhyay, D.; Mishra, D.; Datir, S.; Dhak, P.; Jain, S.; Maiti, T. K.; Basak, A.; Pramanik, P. "Clickable", Trifunctional Magnetite Nanoparticles and their Chemoselective Biofunctionalization. *Bioconjugate Chem.* **2011**, *22*, 1181−1193.

(12) Bolley, J.; Guenin, E.; Lievre, N.; Lecouvey, M.; Soussan, M.; Lalatonne, Y.; Motte, L. Carbodiimide versus Click Cheistry for Nanoparticle Surface Functionalization: A Comprehensive Study for the Elaboration of Multimodal Superparamagnetic Nanoparticles Targeting $\alpha_v\beta_3$ Integrins. *Langmuir* **2013**, *29*, 14639−14647.

(13) Knopp, D.; Tang, D.; Niessner, R. Bioanalytical Applications of Biomolecule-Functionalized Nanometer-Sized Doped Silica Particles. *Anal. Chim. Act.* **2009**, *647*, 14−30.

(14) Jang, W.-D.; Yim, D.; Hwang, I.-H. Photofunctional Hollow Nanocapsules for Biomedical Applications. *J. Mater. Chem. B* **2014**, *2*, 2202−2211.

(15) Perrier, T.; Saulnier, P.; Benoit, J.-P. Methods for the Functionalization of Nanoparticles: New Insights and Perspectives. *Chem.—Eur. J.* **2010**, *16*, 11516−11529.

(16) El-Gamel, N. E. A.; Wortmann, L.; Arroub, K.; Mathur, S. Surface Immobilization and Release of Sparfloxacin Drug from SiO$_2$@Fe$_2$O$_3$ Core-Shell Nanoparticles. *Chem. Commun.* **2011**, *47*, 10076−10078.

(17) Boncel, S.; Zając, P.; Koziol, K. K. K. Liberation of Drugs from Multi-Wall Carbon Nanotube Carriers. *J. Controlled Release* **2013**, *169*, 126−140.

(18) Zhu, Y.; Fang, Y.; Kaskel, S. Folate-Conjugated Fe$_3$O$_4$@SiO$_2$ Hollow Mesoporous Spheres for Targeted Anticancer Drug Delivery. *J. Phys. Chem. C* **2010**, *114*, 16382−16388.

(19) Gua, M.; Que, C.; Wang, C.; Liu, X.; Yan, H.; Liu, K. Multifunctional Superparamagnetic Nanocarriers with Folate and pH-Responsive Targeting Properties for Anticancer Drug Delivery. *Biomaterials* **2011**, *32*, 185−194.

(20) Xiao, L.; Li, J.; Brougham, D. F.; Fox, E. K.; Feliu, N.; Bushmelev, A.; Schmidt, A.; Mertens, N.; Kiessling, F.; Valldor, M.; Fadeel, B.; Mathur, S. Water-Soluble Superparamagnetic Magnetite Nanoparticles with Biocompatible Coating for Enhanced Magnetic Resonance Imaging. *ACS Nano* **2011**, *5*, 6315−6324.

(21) Wu, H.; Gang, L.; Zhang, S.; Zhang, L.; Chen, Y.; Chen, F.; Chen, H. Biocompatibility, MR Imaging and Targeted Drug Delivery of a Rattle-Type Magnetic Mesoporous Silica Nanosphere System Conjugated with PEG and Cancer-Cell-Specific Ligands. *J. Mater. Chem.* **2011**, *21*, 3037−3045.

(22) Yoo, H.; Moon, S.-K.; Hwang, T.; Kim, Y. S.; Kim, J.-H.; Choi, S.-W.; Kim, J. H. Multifunctional Magnetic Nanoparticles Modified with Polyethylenimine and Folic Acid for Biomedical Theracnostics. *Langmuir* **2013**, *29*, 5962−5967.

(23) Hsu, B. Y. W.; Wang, M.; Zhang, Y.; Vijayaragavan, V.; Wong, S. Y.; Chang, A. Y.-C.; Bhakoo, K. K.; Li, X.; Wang, J. Silica−F127

Nanohybrid-Encapsulated Manganese Oxide Nanoparticles for Optimized T_1 Magnetic Resonance Relaxivity. *Nanoscale* **2014**, 6, 293−299.

(24) Pinho, S. L. C.; Pereira, G. A.; Voisin, P.; Kassem, J.; Bouchaud, V.; Etienne, L.; Peters, J. A.; Carlos, L.; Geraldes, C. F. G. C.; Rocha, J.; Deville, M.-H. Fine Tuning of the Relaxometry of γ-Fe_2O_3@SiO_2 Nanoparticles by Tweaking the Silica Coating Thickness. *ACS Nano* **2010**, 4, 5339−5349.

(25) Zhang, M.; Fang, K.; Lin, M.; Hou, B.; Zhong, L.; Zhu, Y.; Wie, W.; Sun, Y. Controlled Fabrication of Iron Oxide/Mesoporous Silica Core−Shell Nanostructures. *J. Phys. Chem. C* **2013**, 117, 21529−21538.

(26) Digigow, R. G.; Dechézelles, J.-F.; Dietsch, H.; Geissbühler, I.; Vanhecke, D.; Geers, C.; Hirt, A. M.; Rothen-Rutishauser, B.; Petri-Fink, A. Preparation and Characterization of Functional Silica Hybrid Magnetic Nanoparticles. *J. Magn. Magn. Mater.* **2014**, 362, 72−29.

(27) Ding, H. L.; Zhang, Y. X.; Wang, S.; Xu, J. M.; Xu, S. C.; Li, G. H. Fe_3O_4@SiO_2 Core/Shell Nanoparticles: The Silica Coating Regulations with a Single Core for Different Core Sizes and Shell Thicknesses. *Chem. Mater.* **2012**, 24, 4572−4580.

(28) Ni, X.; Zheng, Z.; Hu, X.; Xiao, X. Silica-Coated Iron Nanocubes: Preparation, Characterization and Application in Microwave Absorption. *Interface Sci.* **2010**, 341, 18−22.

(29) Rossi, L.; Sacanna, S.; Irvine, W. T. M.; Chaikin, P. M.; Pine, D. J.; Philipse, A. P. Cubic Crystals from Cubic Colloids. *Soft Matter* **2011**, 7, 4139−4142.

(30) Castillo, S. I. R.; Ouhajji, S.; Fokker, S.; Erné, B. H.; Schneijdenberg, C. T. W. M.; Thies-Weesie, D. M. E.; Philipse, A. P. Silica Cubes with Tunable Coating Thickness and Porosity: From Hematite Filled Silica Boxes to Hollow Silica Bubbles. *Microporous Mater.* **2014**, 195, 75−86.

(31) Guerrero-Martinez, A.; Perez-Juste, J.; Liz-Marzan, L. M. Recent Progress on Silica Coating of Nanoparticles and Related Nanomaterials. *Adv. Mater.* **2010**, 22, 1182−1195.

(32) Teng, L.; Xie, J.; Teng, L.; Lee, R. J. Clinical Translation of Folate Receptor-Targeted Therapeutics. *Expert Opin. Drug Delivery* **2012**, 9, 901−908.

(33) Gonen, N.; Assaraf, Y. G. Antifolates in Cancer Therapy: Structure, Activity and Mechanism of Drug Resistance. *Drug Resist. Updates* **2012**, 15, 183−210.

(34) Garcia-Bennett, A.; Nees, M.; Fadeel, B. In Search of the Holy Grail: Folate-Targeted Nanoparticles for Cancer Therapy. *Biochem. Pharmacol.* **2011**, 81, 976−984.

(35) Hilgenbrink, A. R.; Low, P. S. Folate Receptor-Mediated Drug Targeting: From Therapeutics to Diagnostics. *J. Pharm. Sci.* **2005**, 94, 2135−2146.

(36) Low, P. S.; Henne, W. A.; Doorneweerd, D. D. Discovery and Development of Folic-Acid-Based Receptor Targeting for Imaging and Therapy of Cancer and Inflammatory Diseases. *Acc. Chem. Res.* **2008**, 41, 120−129.

(37) Kamaly, N.; Xiao, Z.; Valencia, P. M.; Radovic-Moreno, A. F.; Farokhzad, O. C. Targeted Polymeric Therapeutic Nanoparticles: Design, Development and Clinical Translation. *Chem. Soc. Rev.* **2012**, 41, 2971−3010.

(38) Fisher, R. E.; Siegel, B. A.; Edell, S. L.; Oyesiku, N. M.; Morgenstern, D. E.; Messmann, R. A.; Amato, R. J. Exploratory Study of 99mTc-EC20 Imaging for Identifying Patients with Folate Receptor-Positive Solid Tumors. *J. Nucl. Med.* **2008**, 48, 899−906.

(39) Krais, A.; Wortmann, L.; Hermanns, L.; Feliu, N.; Vather, M.; Stucky, S.; Mathur, S.; Fadeel, B. Targeted Uptake of Folic Acid-Functionalized Iron Oxide Nanoparticles by Ovarian Cancer Cells in the Presence but Not in the Absence of Serum. *Nanomedicine: NBM* **2014**, DOI: 10.1016/j.nano.2014.01.006.

(40) Zheng, Y.; Cheng, Y.; Wang, Y.; Bao, F.; Zhou, L.; Wei, X.; Zhang, Y.; Theng, Q. Quasicubic α-Fe_2O_3 Nanoparticles with Excellent Catalytic Performance. *J. Phys. Chem. B* **2006**, 110, 3093−3097.

(41) Graf, C.; Vossen, D. L. J.; Imhof, A.; van Blaaderen, A. A General Method To Coat Colloidal Particles with Silica. *Langmuir* **2003**, 19, 6693−6700.

(42) Patterson, A. The Scherrer Formula for X-ray Particle Size Determination. *Phys. Rev.* **1939**, 978−982.

(43) Han, Y.-S.; Jeong, G.-Y.; Lee, S.-Y.; Moon, K.-H.; Kim, H.-K. Synthesis of Cubic Type Hollow Silica Particles. *Mater. Lett.* **2009**, 63, 1278−1280.

(44) Jozwiak, W. K.; Kaczmarek, E.; Maniecki, T. P.; Ignaczak, W.; Maniukiewicz, W. Reduction Behavior of Iron Oxides in Hydrogen and Carbon Monoxide Atmospheres. *Appl. Catal., A* **2007**, 326, 17−27.

(45) Murad, E.; Johnston, J. Iron Oxides and Oxyhydroxide. In *Mössbauer Spectroscopy Applied to Inorganic Chemistry*; Long, G., Ed.; Plenum Publ. Corp.: New York, 1987; pp 582−707.

(46) Mahmed, N.; Heczke, O.; Lancok, H.; Hannula, S.-P. The Magnetic and Oxidation Behavior of Bare and Silica-Coated Iron Oxide Nanoparticles Synthesized by Reverse Co-Precipitation of Ferrous Ion (Fe^{2+}) in Ambient Atmosphere. *J. Magn. Magn. Mater.* **2014**, 353, 15−22.

(47) Gai, S.; Yang, P.; Li, C.; Wang, W.; Dai, Y.; Niu, N.; Lin, J. Synthesis of Magnetic, Up-Conversion Luminescent, and Mesoporous Core−Shell-Structured Nanocomposites as Drug Carriers. *Adv. Funct. Mater.* **2010**, 20, 1166−1172.

(48) Diederich, T.; Dybowska, A.; Schott, J.; Valsami-Jonas, E.; Oelkers, E. H. The Dissolution Rates of SiO_2 Nanaoparticles as a Function of Particle Size. *Environ. Sci. Technol.* **2012**, 46, 4909−4915.

(49) York, A. W.; Zhang, Y.; Holley, A. C.; Guo, Y.; Huang, F.; McCormick, C. L. Facile Synthesis of Multivalent Folate-Block Copolymer Conjugates via Aqueous RAFT Polymerization: Targeted Delivery of siRNA and Subsequent Gene Suppression. *Biomacromolecules* **2009**, 10, 936−943.

(50) Aviva, O.; Horowitz, T.; Gabizon, A.; Gibson, D. Folate-Targeted PEG as a Potential Carrier for Carboplatin Analogs. Synthesis and in Vitro Studies. *Bioconjugate Chem.* **2003**, 14, 563−574.

(51) Pratt, A. R.; Muir, I. J.; Nesbit, H. W. X-ray Photoelectron and Auger Electron Spectroscopic Studies of Pyrrhotite and Mechanism of Air Oxidation. *Geochim. Cosmochim. Acta* **1994**, 59, 827−841.

(52) Waddell, T. G.; Leyden, D. E.; Debello, M. T. The Nature of Organosilane to Silica-Surface Bonding. *Science* **1981**, 103, 5303−5307.

(53) Zhang, X.; Niu, Y.; Li, Y.; Li, Y.; Zhao, L. Preparation and Thermal Stability of the Spindle α-Fe_2O_3@SiO_2 Core−Shell Nanoparticles. *J. Solid State Chem.* **2014**, 211, 69−74.

(54) He, Y. Y.; Wang, X. C.; Jin, P. K.; Zhao, B.; Fan, X. Ionically Self-Assembled Terephthalylidene-bis-4-n-alkylanilines/n-decanesulfonic Acid Supramolecules: Synthesis, Mesomorphic Behaviour and Optical Properties. *Spectrochim. Acta, Part A* **2009**, 72, 876−879.

(55) Pueng, H.; Bao, L.; Zhang, C.; Lin, J.; Luo, T.; Yang, D.; He, M.; Li, Z.; Gao, G.; Gao, B.; Fheng, S.; Cui, D. Folic Acid-Conjugated Silica-Modified Gold Nanorods for X-ray/CT Imaging-Guided Dual-Mode Radiation and Photo-Thermal Therapy. *Biomaterials* **2011**, 32, 9796−9809.

(56) Shang, L.; Nienhaus, K.; Nienhaus, G. U. Engineering Interaction with Cells: Size Matters. *J. Nanobiotechnol.* **2014**, 12, 5.

(57) Hühn, D.; Kantner, K.; Geidel, C.; Brandholt, S.; Cock, I. D.; Soenen, S. J. H.; Rivera-Gil, P.; Montenegro, J.-M.; Braeckmans, K.; Müllen, K.; Nienhaus, G. U.; Klapper, M.; Parak, W. J. Polymer-Coated Nanoparticles Interaction with Proteins and Cells: Focusing on the Sign of the Net Charge. *ACS Nano* **2013**, 7, 3253−3263.

(58) Sahoo, B.; Devi, K. S. P.; Sahu, S. K.; Nayak, S.; Maiti, T. K.; Dhara, D.; Pramanik, P. Facile Preparation of Multifunctional Hollow Silica Nanoparticles and Their Cancer Specific Targeting Effect. *Biomater. Sci.* **2013**, 1, 647−657.

(59) Yang, S.; Xu, Y.; Sun, Y.; Zhang, G.; Gao, D. Size-Controlled Synthesis, Magnetic Property, and Photocatalytic Property of Uniform α-Fe_2O_3 Nanoparticles via a Facile Additive-Free Hydrothermal Route. *CrystEngComm* **2012**, 14, 7915−7921.

(60) Cornell, R. M.; Schwertmann, U. *The Iron Oxides: Structure, Properties, Reactions, Occurrence and Uses*, 1st ed, VCH: New York, 1996.

(61) Krug, H. F.; Wick, P. Nanotoxicology: An Interdisciplinary Challenge. *Angew. Chem., Int. Ed.* **2011**, *50*, 1260−1278.

(62) Shi, J.; Karlsson, H. L.; Johansson, K.; Gogavadze, V.; Xiao, L.; Li, J.; Burks, T.; Garcia- Bennett, A.; Uheida, A.; Muhammed, M.; Mathur, S.; Morgenstern, R.; Kagan, V. E.; Fadeel, B. Microsomal Glutathione Transferase 1 Protects against Toxicity Induced by Silica Nanoparticles but Not by Zinc Oxide Nanoparticles. *ACS Nano* **2012**, *6*, 1925−1938.

(63) Xia, X. R.; Monteiro-Riviere, N. A.; Mathur, S.; Song, X.; Xiao, L.; Oldenberg, S. J.; Fadeel, B.; Riviere, J. E. Mapping the Surface Adsorption Forces of Nanomaterials in Biological Systems. *ACS Nano* **2011**, *5*, 9074−9081.

(64) Murray, A. R.; Kisin, E.; Imman, A.; Young, S.-H.; Muhammed, M.; Burks, T.; Uheida, A.; Tkach, A.; Rivere, J. E.; Monteiro-Rivere, N.; Shvedova, A. A. Oxidative Stress and Dermal Toxicity of Iron Oxide Nanoparticles In Vitro. *Cell. Biochem. Biophys.* **2013**, *67*, 461−476.

(65) Laaksonen, T.; Santos, H.; Vihola, H.; Salonen, J.; Riikonen, J.; Heikkilä, T.; Peltonen, L.; Kumar, N.; Murzin, D. Y.; Letho, V.-P.; Hirvonen, J. Failure of MTT as a Toxicity Testing Agent for Mesoporous Silicon Microparticles. *Chem. Res. Toxicol.* **2007**, *20*, 1913−1918.

(66) Oostingh, G. J.; Casals, E.; Italiani, P.; Colognato, R.; Strizinger, R.; Ponti, J.; Pfaller, T.; Kohl, Y.; Ooms, D.; Favilli, F.; Leepens, H.; Lucchesi, D.; Rossi, F.; Nelissen, I.; Thielecke, H.; Puntes, V. F.; Duschl, A.; Boraschi, D. Problems and Challenges in the Development and Validation of Human Cell-Based Assays To Determine Nano-particle-Induced Immunomodulatory Effects. *Part. Fibre Toxicol.* **2011**, *8*, 1−21.

(67) Monteiro-Riviere, N. A.; Inman, A. O.; Zhang, L. W. Limitations and Relative Utility of Screening Assays To Assess Engineered Nanoparticle Toxicity in a Human Cell Line. *Toxicol. Appl. Pharmacol.* **2009**, *234*, 222−235.

16642

dx.doi.org/10.1021/am503068r | *ACS Appl. Mater. Interfaces* 2014, 6, 16631−16642